Research Article

Optimal bandwidth and systematic error of full-Stokes micropolarizer arrays

ANDREY S. ALENIN,* ISRAEL J. VAUGHN, AND J. SCOTT TYO

School of Engineering and Information Technology, University of New South Wales, Canberra, ACT 2610, Australia
**Corresponding author: a.alenin@adfa.edu.au*

In this paper, we present the first in-depth analysis of the bandwidth tradeoffs, error performance, and noise resiliency of full-Stokes micropolarizer array (MPA) designs. By applying our Fourier domain tools that provide a systematic way for arranging information carriers and allocating bandwidth, we develop a number of new full-Stokes MPA layouts and compare them to the existing full-Stokes MPAs in the literature, all of which use 2 × 2 pixel unit cells to build the MPA. We compare the reconstruction accuracy afforded by these traditional designs with the generalized 2 × *L* family of MPAs, a 3 × 3 tiling, as well as a 2 × 2 × 3 layout that uses multiple snapshots and trades off temporal resolution for spatial resolution. Of those systems, the hybrid spatiotemporally modulated 2 × 2 × 3 MPA provisions the most bandwidth and provides the highest reconstruction accuracy, while the modified 2 × *L* family remains the best performing single-snapshot MPA. Additionally, we study the degradation of reconstruction accuracy under the presence of systematic error in MPA fabrication. We find that reducing the amount of correlated error is by far the largest factor in ensuring robust performance.

OCIS codes: (110.5405) Polarimetric imaging; (260.5430) Polarization; (120.5410) Polarimetry.

https://doi.org/10.1364/AO.57.002327

1. INTRODUCTION

Modulated polarimeters determine the optical polarization state by multiplexing a set of polarization-dependent sidebands, usually in an orthogonal frequency division multiplexed sense onto a detector's given bandwidth. These sidebands are created by optical elements whose polarization properties vary (usually periodically) as a function of an independent variable of the system [1], such as time [2,3], space [4,5], wavelength [6], angle of incidence [7], or even combinations of multiple independent variables [8,9]. Polarimeters can be active (Mueller) or passive (Stokes), but the same principles can describe both [10]. Because polarimeters use the bandwidth of a single set of detectors to measure multiple pieces of information, they inherently give up resolution relative to a non-polarimetric imager using the same set of detectors.

Traditionally, polarimeters have been described by the data reduction matrix (DRM) method [2], and their optimization has generally been in terms of system conditioning and signal-to-noise ratio (SNR) for zero-bandwidth systems [11–13]. However, with the recent description of modulated polarimeters in terms of information channels [1], interest is growing in using bandwidth to describe and quantify their performance. The question of how much bandwidth is needed for a given information channel and how to allocate it most effectively within the total channel structure is difficult to address for the most general case. In this paper, we limit our focus to the class of division of focal plane (DoFP) polarimeters [14]. The underlying micropolarizer array (MPA) that enables the polarization sensitivity means that such polarimeters can be treated as channeled ones [10]. The first MPA was introduced by Chun [15], and that layout is still being used by many [16] despite clear limitations that have since been described. The need to consider bandwidth tradeoffs in polarimeter design was realized by Tyo, LaCasse, and colleagues [1,4,17], while LeMaster and Hirakawa were the first to apply it to the MPA design [18]. Since then, we showed that the spatial frequency carrier locations within their 2 × 4 MPA are extendable into a family of 2 × *L* MPAs that open the door for further balancing of the bandwidth provided, and the reconstruction quality achieved [19].

Most MPAs are only sensitive to linear polarization parameters, and virtually all rigorous analyses consider only linear MPAs. In this paper, we leverage a set of general tools that we developed for arbitrary focal planes [10,20] to provide the first in-depth treatment of MPA designs that can measure all four Stokes parameters, such as those introduced by Zhao and colleagues [21], by Bachman and Peltzer [22,23], as well as by Myhre, Hsu, Pau, and colleagues [24,25]. We compare the

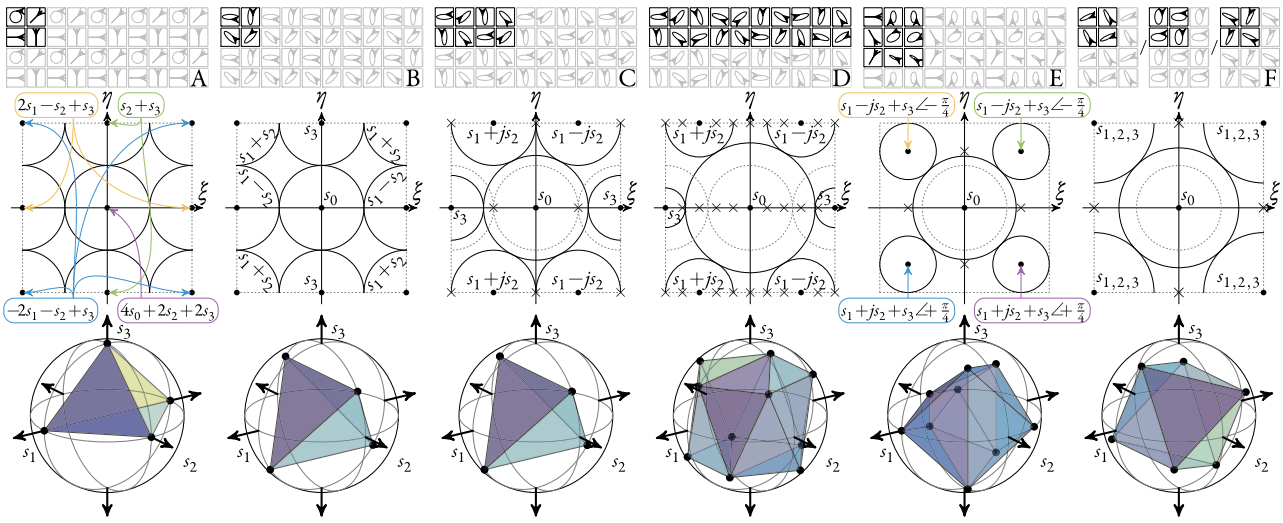

Fig. 1. MPAs. Top row: A, Bachman's 2 × 2; B, Myhre's 2 × 2; C, this work's 2 × 4; D, this work's 2 × 10; E, this work's 3 × 3; F, Alenin's 2 × 2 × 3. Middle row: Fourier domains with •/× indicating filled and empty channel centers, respectively, as contained within the corresponding $\underline{\tilde{\mathbf{A}}}$; solid lines outline the allocated channel bandwidths, while dotted lines outline the allocated s_0 bandwidth of Bachman's and Myhre's MPAs. The $\angle\phi$ in E denotes the complex angle in $e^{j\phi}$. Bottom row: the volume enclosed within the Poincaré sphere by the analyzing vectors.

performance of these demonstrated full-Stokes MPAs to a number of new designs presented here.

A. Conventional Polarimetry

Stokes parameters are commonly used to describe the polarization of incoherent light and are formed into a vector [14],

$$\begin{aligned}\underline{\mathbf{S}} &= [s_0 \quad s_1 \quad s_2 \quad s_3]^{\mathrm{T}} \\ &= [I_H + I_V \quad I_H - I_V \quad I_{+45} - I_{-45} \quad I_R - I_L]^{\mathrm{T}}. \end{aligned} \tag{1}$$

The latter three parameters represent differential irradiance measurements between pairs of orthogonal states and lie inside the Poincaré sphere; $s_0 \geq \sqrt{s_1^2 + s_2^2 + s_3^2}$. To estimate Stokes parameters, indirect measurements are made by passing light of an unknown polarization state $\underline{\mathbf{S}}$ through a series of predetermined analyzing polarization states $\underline{\mathbf{A}}_n$. By grouping N measurements together and assuming that the Stokes parameters are constant for these measurements,

$$\begin{aligned}\underline{\mathbf{I}} &= [I_1 \quad \cdots \quad I_N]^{\mathrm{T}} = [\underline{\mathbf{A}}_1^{\mathrm{T}}\underline{\mathbf{S}} \quad \cdots \quad \underline{\mathbf{A}}_N^{\mathrm{T}}\underline{\mathbf{S}}]^{\mathrm{T}} + \vec{\mathbf{n}} \\ &= \underline{\underline{\mathbf{W}}}\,\underline{\mathbf{S}} + \vec{\mathbf{n}}. \end{aligned} \tag{2}$$

We can estimate the Stokes parameters by calculating the pseudo-inverse $\underline{\underline{\mathbf{W}}}^{+}$ and applying the DRM,

$$\underline{\mathbf{S}} = \underline{\underline{\mathbf{W}}}^{+}\underline{\mathbf{I}} = \underline{\underline{\mathbf{W}}}^{+}\underline{\underline{\mathbf{W}}}\,\underline{\mathbf{S}} + \underline{\underline{\mathbf{W}}}^{+}\vec{\mathbf{n}}, \tag{3}$$

where $\vec{\mathbf{n}}$ represents additive detector noise.

Currently, most MPAs are limited to reconstructing the first three Stokes parameters. However, the difficulty of constructing pixels sensitive to circular polarization is slowly being alleviated as manufacturing improves. Zhao and colleagues were the first to implement a full-Stokes MPA [21] by placing liquid crystals on top of each pixel with varying amounts of twist angle in a 2 × 2 unit cell arrangement. Their design effectively replaced one of the pixels of Chun's MPA with a right circularly polarized sensing filter, thus resulting in the R/0/45/90 MPA. Later, Bachman and Peltzer arrived at a similar layout that achieved circular polarization sensitivity by building spiral plasmonic antenna-like structures on top of each pixel [22,23]. The two permutations offer identical performance; the permutation analyzed in this paper more closely resembles Bachman's MPA, shown in Fig. 1A. Soon after, Myhre, Hsu, Pau, and colleagues [24,25] brought full-Stokes MPAs closer to a practicable realization through their approach of patterning birefringent polymers on top of micropolarizers. They proposed a number of MPAs; however, their designs did not optimize for maximum Stokes channel bandwidth and, instead, optimized for minimum condition number (CN) of the unit cell's $\underline{\underline{\mathbf{W}}}$. The result is the familiar regular tetrahedra inscribed within the Poincaré sphere [11–13]. Their designs included the straightforward application of $\delta = \cos^{-1}(-2/3)$ linear retarders at ±15.1° and ±51.7° on top of a non-patterned linear polarizer [12], as well as the MPA, where the polarizer layer is patterned with Chun's conventional 0/45/90/135 orientations, while $\delta = \frac{1}{2}\cos^{-1}(1/3)$ linear retarders are aligned at 135/90/45/0 on top. The latter of the two MPAs is considered in this paper and can be seen in Fig. 1B. Recent work has even combined MPAs with color filter arrays (CFAs) [26], and, while that problem is beyond the scope of this work, the methods developed in our previous work [20] could be used to extend this work for more optimal CFA integration.

B. Channeled Description

We recently developed a general set of Fourier domain tools for designing channeled focal plane arrays (FPAs) [10,19,20], and here we employ them to look at a number of full-Stokes MPA designs with the goal of identifying those that yield optimal bandwidth. In Eq. (2), Stokes parameters are assumed to be constant; to incorporate it as being a function of position, we expand I_n into a sampled two-dimensional (2D) scene

$I(x_n, y_n)$. Taking its Fourier transform $\tilde{I}(\xi, \eta)$, we identify the channel structure $\mathcal{F}\{\underline{\mathbf{C}}\}$, where $\underline{\mathbf{C}}$ is a length $2M+1$ vector that lists the channels, and M is the number of independent modulation functions [10]. We can determine a $(2M+1) \times 4$ matrix $\underline{\underline{\mathbf{Q}}}$,

$$\mathcal{F}\{\underline{\mathbf{C}}\} = \underline{\underline{\mathbf{Q}}}\mathcal{F}\{\underline{\mathbf{S}}\} = \left[\underline{\mathbf{q}}_{\xi,\eta;s_0} \quad \underline{\mathbf{q}}_{\xi,\eta;s_1} \quad \underline{\mathbf{q}}_{\xi,\eta;s_2} \quad \underline{\mathbf{q}}_{\xi,\eta;s_3}\right]\mathcal{F}\{\underline{\mathbf{S}}\}, \tag{4}$$

which relates the channel structure to the Fourier transform of the Stokes parameters. In Eq. (4), $\underline{\mathbf{q}}_{\xi,\eta;s_i}$ describes how the Stokes parameters are distributed in the polarimeter's channel structure. Similar to the DRM method in Eq. (2), we can reconstruct $\underline{\mathbf{S}}$ by inverting the process,

$$\underline{\mathbf{S}} = \mathcal{F}^{-1}\{\underline{\underline{\mathbf{Q}}}^{+}\mathcal{F}\{\underline{\mathbf{C}}\}\}, \tag{5}$$

where $\underline{\underline{\mathbf{Q}}}^{+}$ is the pseudo-inverse.

2. FULL-STOKES MICROPOLARIZER ARRAYS

A. 2 × L Family of MPAs

The modified $2 \times L$ family of full-Stokes MPAs is a potent, but non-obvious, follow-on to the $2 \times L$ family we introduced previously for linear MPAs [19]. Its analyzing vector is

$$\underline{\mathbf{A}} = \frac{1}{2}\begin{bmatrix} 1 \\ \sqrt{2/3}\cos(am\pi)\cos(bn\pi) \\ \sqrt{2/3}\sin(am\pi)\cos(bn\pi) \\ \sqrt{1/3}\cos(m\pi) \end{bmatrix}, \tag{6}$$

where m and n are integer pixel coordinates, while a and b are the carrier frequencies in x and y in cycles per pixel, respectively. The modification from Eq. (5) in our 2017 Optics Letter [19] is the addition of an s_3 carrier, which requires the reduction of signal in s_1 and s_2 by a factor of $\sqrt{2/3}$ to ensure the optimal CN of $\sqrt{3}$ for $\underline{\underline{\mathbf{W}}}$. We assume that each pixel is composed of a cascaded linear retarder (LR) with fast axis orientation θ_{LR} and retardance δ_{LR} and linear polarizer (LP) with orientation θ_{LP}. The following patterning is one of the many possible permutations that achieve the desired analyzing vector of Eq. (6):

$$\theta_{\mathrm{LP}}(m, n) = \mathrm{mod}(am\pi/2 + bn\pi/2, \pi), \tag{7a}$$

$$\theta_{\mathrm{LR}}(m, n) = \mathrm{mod}(3\pi/4 - (1-a)m\pi/2 - bn\pi/2, \pi), \tag{7b}$$

$$\delta_{\mathrm{LR}}(m, n) = \cos^{-1}(1/3)/2. \tag{7c}$$

The retarders' θ_{LR} is patterned as complementary of the a parameter—this is done to place the s_3 carrier at the Nyquist boundary in ξ. As a result, the modified $2 \times L$ family benefits greatly from having an even L. For a hypothetical odd L, you would be required to make a choice between having non-unity degree of polarization (DoP) analysis states or having a set of harmonic s_3 channels that interfere together and reduce the available bandwidth. Avoiding the choice altogether by enforcing an even L is a sensible approach. Note that there is an important distinction between the scenarios when $L/2$ is odd and when it is even. In the former, we will have $2L$ different analyzing vectors, whereas in the latter, we will only have L different analyzing vectors, which could translate into cost savings.

For the even L case, we use the frequency phase matrix [10] to obtain the channel structure,

$$\tilde{\underline{\mathbf{A}}} = \begin{bmatrix} \frac{1}{2}\delta(\xi, \eta) \\ \frac{1}{4\sqrt{6}}\left[+\delta\left(\xi - \frac{a}{2}, \eta \pm \frac{b}{2}\right) + \delta\left(\xi + \frac{a}{2}, \eta \pm \frac{b}{2}\right)\right] \\ \frac{j}{4\sqrt{6}}\left[-\delta\left(\xi - \frac{a}{2}, \eta \pm \frac{b}{2}\right) + \delta\left(\xi + \frac{a}{2}, \eta \pm \frac{b}{2}\right)\right] \\ \frac{1}{4\sqrt{3}}\left[+\delta\left(\xi - \frac{1}{2}, 0\right) + \delta\left(\xi + \frac{1}{2}, 0\right)\right] \end{bmatrix}, \tag{8}$$

which nominally has seven non-empty channels with a and b determining the overall positioning of carriers. We will consider two members of this family in greater detail: the 2×4 MPA with $a = 1/2$, and $b = 1$, as shown in Fig. 1C, as well as the 2×10 MPA with $a = 3/5$, and $b = 1$, as shown in Fig. 1D.

B. 3 × 3 MPA

The 3×3 MPA shown in Fig. 1E has the following analyzing vector:

$$\underline{\mathbf{A}} = \frac{1}{2}\begin{bmatrix} 1 \\ \cos(2m\pi/3)\cos(2n\pi/3) \\ \cos(2m\pi/3)\sin(2n\pi/3) \\ \sin(2m\pi/3)\cos(2n\pi/3 + 45°) \end{bmatrix}. \tag{9}$$

It can be accomplished with the following 3×3 pattern:

$$p_{3\times3} = \begin{bmatrix} 1 & \sqrt{5/8} & \sqrt{5/8} \\ 1 & \sqrt{5/8+\alpha} & \sqrt{5/8+\alpha} \\ 1 & \sqrt{5/8-\alpha} & \sqrt{5/8-\alpha} \end{bmatrix}, \tag{10a}$$

$$\psi_{3\times3} = \begin{bmatrix} 0° & -90° & -90° \\ -60° & 30° & 30° \\ 60° & -30° & -30° \end{bmatrix}, \tag{10b}$$

$$\chi_{3\times3} = \frac{1}{2}\tan^{-1}\begin{bmatrix} 0 & -\sqrt{3/2} & +\sqrt{3/2} \\ 0 & +\sqrt{3/2+\beta} & -\sqrt{3/2+\beta} \\ 0 & -\sqrt{3/2-\beta} & +\sqrt{3/2-\beta} \end{bmatrix}, \tag{10c}$$

where $\alpha = 3\sqrt{3}/16$, and $\beta = \sqrt{3}/2$, while p, 2ψ, and 2χ correspond to the spherical coordinates within the Poincaré sphere as a DoP, azimuthal angle, and polar angle, respectively. The azimuthal angle corresponds to the micropolarizer orientations, while the microretarder parameters that result in $\chi_{3\times3}$ can be achieved with the following patterning:

$$\theta_{\mathrm{LR}} = \begin{bmatrix} 0° & 135° & 45° \\ 0° & 165° & 75° \\ 0° & 15° & 105° \end{bmatrix}, \tag{11a}$$

$$\delta_{\mathrm{LR}} = \begin{bmatrix} 0° & 50.77° & 50.77° \\ 0° & 59.13° & 59.13° \\ 0° & 24.15° & 24.15° \end{bmatrix}. \tag{11b}$$

Its corresponding channel structure is

$$\underline{\tilde{\mathbf{A}}} = \begin{bmatrix} \frac{1}{2}\delta(\xi,\eta) \\ \frac{1}{8}\left[+\delta\left(\xi \pm \frac{1}{3}, \eta - \frac{1}{3}\right) + \delta\left(\xi \pm \frac{1}{3}, \eta + \frac{1}{3}\right)\right] \\ \frac{j}{8}\left[-\delta\left(\xi \pm \frac{1}{3}, \eta - \frac{1}{3}\right) + \delta\left(\xi \pm \frac{1}{3}, \eta + \frac{1}{3}\right)\right] \\ \frac{1+j}{8\sqrt{2}}\left[-j\delta\left(\xi \pm \frac{1}{3}, \eta - \frac{1}{3}\right) + \delta\left(\xi \pm \frac{1}{3}, \eta + \frac{1}{3}\right)\right] \end{bmatrix}. \quad (12)$$

This 3 × 3 MPA is unique in this paper, as it is the only one having non-unity DoP states, which are necessary to "sample" the carrier-producing periodic functions properly. For all other MPAs in this paper, the sampling of the carrier-producing periodic functions falls onto the peaks, resulting in pure states. If one was to ignore Eq. (10a) and make all states purely polarized, the channel structure shown in Fig. 1E would no longer hold—the indicated empty channels would be populated, reducing the system's bandwidth. Although having non-unity DoP states is a disadvantage compared to other systems [27,28], the system's performance is a combination of noise, bandwidth, and system error considerations. Combined with it having non-optimal DRM, inclusion of the 3 × 3 MPA specifically tests the relative importance of bandwidth.

C. Multi-snapshot Systems

We extend the multi-snapshot linear MPAs from our previous work to full-Stokes systems. At the base is the original $2 \times L$ family [19] with $a = b = 1$, resulting in a simple 0/90/90/0 MPA that only has channels located in the corners of the Fourier plane. We put a $\delta = 126.32°$ linear retarder in front and cycle it through three orientations, $\theta = \{15.66°, 45.00°, 74.34°\}$. These values differ from our previous work; the new solution was chosen for its even steps in the orientations, making implementation more practical. We call this polarimeter the 2 × 2 × 3 MPA, and it can be seen in Fig. 1F. The analyzing vectors inscribe a regular octahedron. To be fair in comparisons with other MPAs, special care is required—the exposure time is split into three parts, and each one receives a noise contribution with the variance scaled by 1/3. This family of systems trades off temporal bandwidth for spatial bandwidth and thereby enables maximum separation of polarization-carrying sidebands and intensity-carrying basebands. This modulation scheme represents an alternative view to Vaughn's hybrid modulated fast-Stokes polarimeter [29]. Instead of taking the Fourier Transform of all the modulation dimensions, including temporal, we directly combine three discrete snapshots, as advocated in our original work on channeled polarimeters [10].

3. SYSTEM PERFORMANCE

A. Reconstruction Accuracy

Carrier design, data bandwidth, bandwidth allocation, channel population, and channel unmixing all play a role in reconstruction accuracy. Table 1 details the channel unmixing performance. However, to evaluate the performance of an MPA while taking bandwidth into account, we need to look further than the equally weighted variance (EWV) dictated by $\underline{\underline{\mathbf{Q}}}^{+}$ and instead simulate how the MPA measures realistic data. Figure 2 shows the infrared hyperspectral imaging polarimeter (IHIP) data we use for this exercise [30]. For 32 independent instantiations of each noise level between 9 dB and 36 dB in mean SNR, we perform two particle-swarm optimizations: (a) up-to-sixteen parameters $\{r_0, r_1, r_2, r_3, \varepsilon_0, \varepsilon_1, \varepsilon_2, \varepsilon_3\}_{s/b}$, defining filters to maximize DoP accuracy; (b) up-to-four parameters, $\{r_0, \varepsilon_0\}_{s/b}$, defining filters to maximize s_0 accuracy. The s and b subscripts denote side and baseband, respectively. The distinction was only necessary for Bachman's MPA, as its $\underline{\underline{\mathbf{Q}}}^{+}$ requires the use of both base and sideband channels to reconstruct s_0. All other MPAs isolate s_0 to the baseband, thus resulting in fewer parameters to optimize over. We quantify reconstruction accuracy with peak SNR (PSNR) [31], which is related to mean squared error (MSE) as

Table 1. Notable Full-Stokes Micropolarizer Array Patterns[a]

Origin	Size	a	b	N	CN	$\sigma^2_{0,1,2,3}$	$\underline{\underline{\mathbf{Q}}}^{T}$	$\underline{\underline{\mathbf{Q}}}^{+}$
Bachman [22]	2 × 2	–	–	1	3.23	3,6,14,14	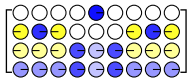	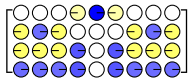
Myhre [24]	2 × 2	–	–	1	$\sqrt{3}$	$1, \frac{9}{2}, \frac{9}{2}, 6$	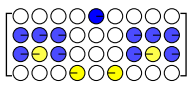	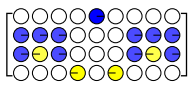
This Work	2 × 4	1/2	1	1	$\sqrt{3}$	1,6,6,6	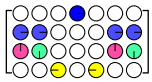	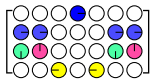
This Work	2 × 10	3/5	1	1	$\sqrt{3}$	1,6,6,6		
This Work	3 × 3	2/3	2/3	1	2	1,4,4,4	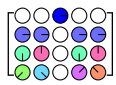	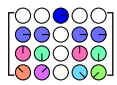
Alenin [19]	2 × 2 × N	1	1	3	$\sqrt{3}$	$\frac{1}{3}$, 4, 4, 4	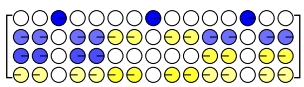	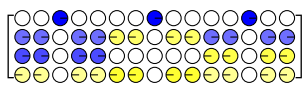

[a]CN is the condition number of the unit cell's $\underline{\underline{\mathbf{W}}}$. $\sigma^2_{0,1,2,3}$ are the noise variances for each Stokes parameter from $\underline{\underline{\mathbf{Q}}}$; their sum is an EWV. The circles represent the polar form of the coefficients—the direction of the radius line contains the phase information as right = +1, up = +j, left = 1, down = j. Empty circles indicate that a given Stokes parameter does not map onto a given channel; an empty channel would be a vertical set of circles in $\underline{\underline{\mathbf{Q}}}^{T}$ and $\underline{\underline{\mathbf{Q}}}^{+}$; they are omitted for brevity.

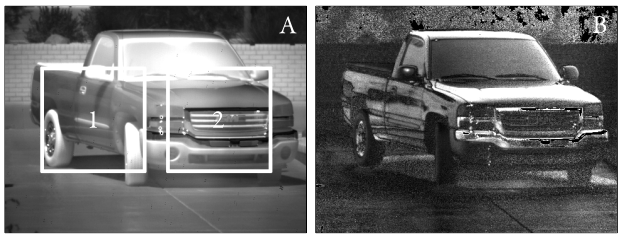

Fig. 2. IHIP mid-wavelength infrared (MWIR) data, $\lambda = 3848$ nm. A, s_0. B, DoP.

$$\mathrm{PSNR} = 10\log_{10}(\mathrm{MAX}^2/\mathrm{MSE}), \tag{13}$$

where MAX = 1 for normalized s_0 and DoP. The respective r_i and ε_i parameters define the Planck-taper filter for s_i: unity near the center, zero on the outside, and the falloff range;

$$H(\varepsilon_i r_i \le r \le r_i) = \frac{1}{1+\exp\left(-2\varepsilon_i r_i\left[\frac{1}{r-\varepsilon_i r_i}+\frac{1}{r-r_i}\right]\right)}. \tag{14}$$

The filters are centered around the corresponding delta functions in $\underline{\underline{\mathbf{Q}}}$. Figure 3 shows reconstructed and absolute error images for a single noise instantiation of the 32 that were averaged to achieve the final accuracy results shown in Fig. 4.

For low SNRs, the optimized filters are narrow, thus limiting the reconstruction quality by the CN of the DRM and the EWV of the channel structure. For higher SNRs, the optimized filters widen to the point where the frequency content of a given Stokes parameter remains higher than the noise floor, as well as the aliasing frequencies of adjacent channels.

B. Systematic Error

The effect that the noise floor and the channel proximity have on the reconstruction accuracy achieved by each MPA is even more evident when you consider systematic error. The analysis is based on the same system evaluation function as the one used in Section 3.A with the addition of imperfections to $\underline{\mathbf{A}}$ of each pixel and the corresponding change to $\underline{\underline{\mathbf{Q}}}$. In principle, $\underline{\underline{\mathbf{Q}}}$ can be adjusted both in terms of channel coefficients and introduction of new channels within the non-local reconstruction paradigm. However, because of the latter effect's overall negligible contribution to channel crosstalk, it is not accounted for in the reconstructions here. Further distinctions in the way of reintroducing local reconstruction may be beneficial, but that discussion is outside the scope of this work. For this exercise, we perform 980 particle-swarm optimizations—DoP and s_0 reconstructions for ten MPA configurations, as enumerated in Table 2 and visualized in Fig. 5. We consider seven standard deviation levels (1/8°, 1/4°, 1/2°, 1°, 2°, 4°, 8°) within two independently introduced systematic error sources: (a) pixel-independent angle and retardance; and (b) mask-correlated angle and retardance. This distinction is introduced to study both the effects of increasing of the noise floor [error source (a)], as well as the introduction of unintended channels [error source (b)]. Each optimization's function evaluation is a result of the averaging of 25 noise instantiations and 25 systematic error

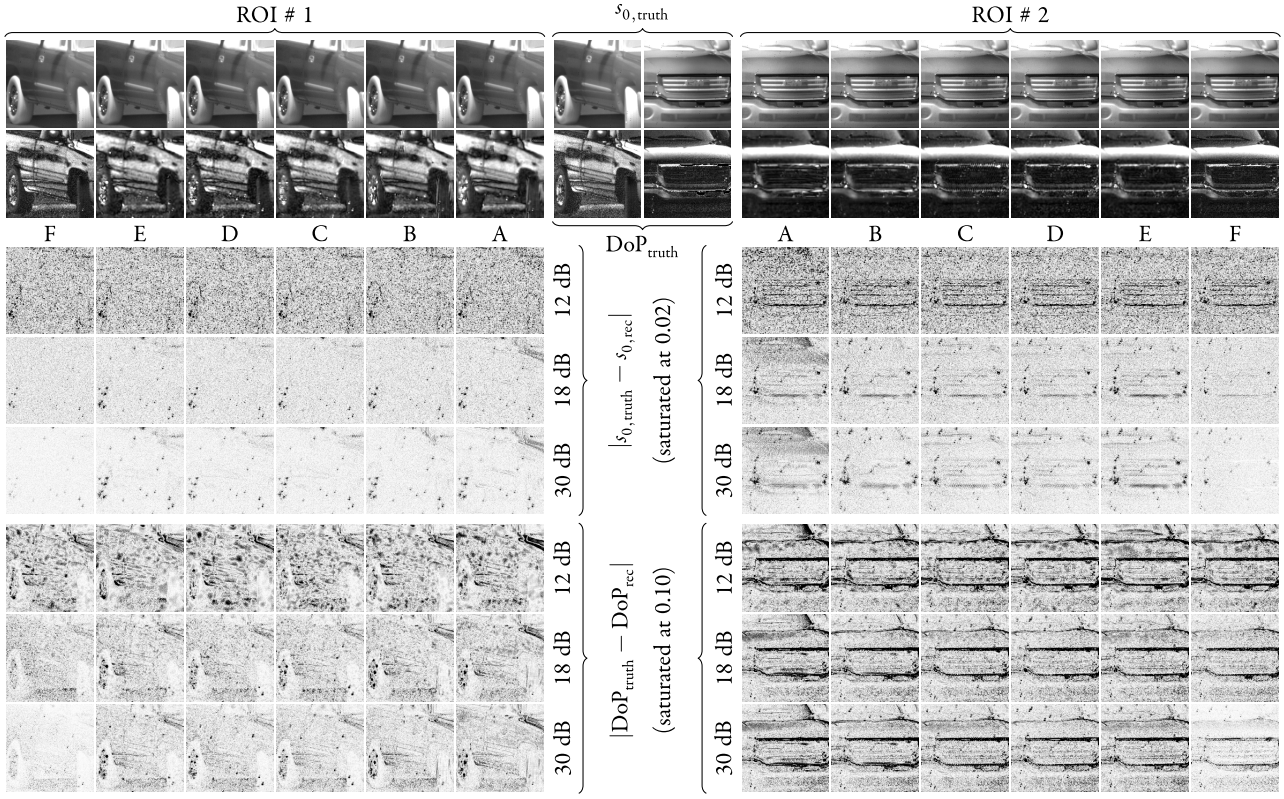

Fig. 3. Reconstructed images. Top two rows: the inside 2 × 2 grid shows the true s_0 and DoP; the outside shows the reconstructed s_0 and DoP at SNR = 30 dB. Bottom six rows: absolute error between reconstructed images and truth. MPA labels and regions of interest (ROIs) are consistent with Figs. 1 and 2, respectively.

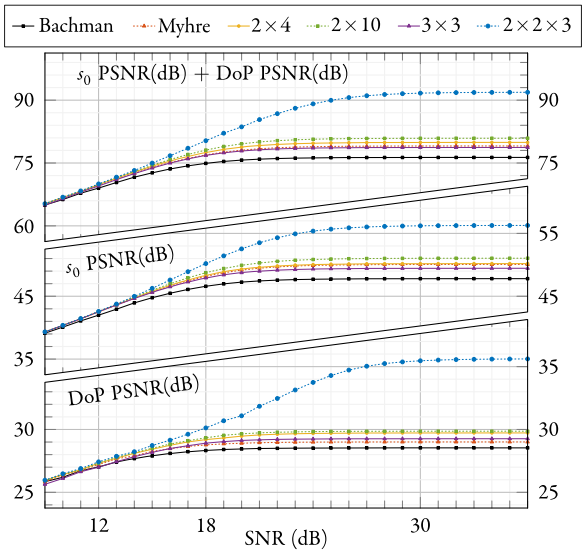

Fig. 4. Attainable reconstruction quality of MPAs shown in Fig. 1.

Table 2. MPA Error Enumeration[a]

MPA	Configuration	θ_{LP}	θ_{LR}	δ_{LR}	Total
Bachman	1	4	1	1	6
Myhre	1	4	4	4	12
2 × 4	1	4	4	4	12
	2	8	8	8	24
2 × 10	1	10	10	10	30
	2	20	20	20	60
3 × 3	1	6	6	6	18
	2	9	6	6	21
2 × 2 × 3	1	2	3	1	6
	2	4	3	1	8

[a]The number of errors follows the number of uncertain parameters added by each polarizer/retarder mask. Configurations are consistent with Fig. 5.

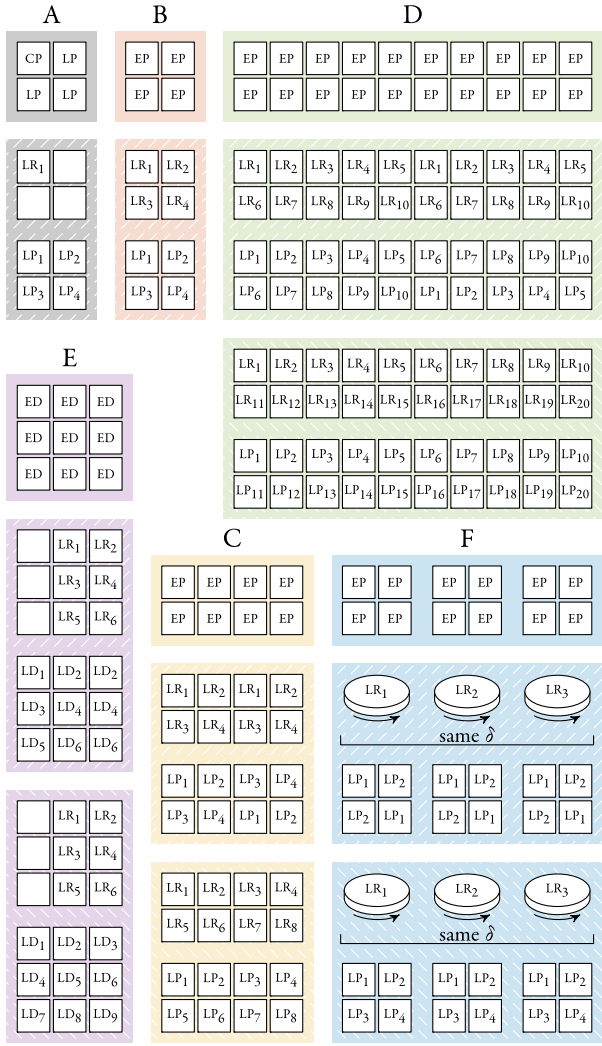

Fig. 5. MPA pixel configurations (letter indices are consistent with Figs. 1 and 3). Pixel labels refer to the lithographic layers: L, linear; C, circular; E, elliptical; P, polarizer; R, retarder; D, diattenuator. Each polarization element's subscript refers to the mask number from which it is produced. Northeast and northwest background hashing refer to Configurations 1 and 2, respectively.

instantiations combined without permutations. In order to speed up optimization convergence, we use the final parameter sets of each MPA found in the previous section as the initial population.

Because the 2 × 2 × 3 MPA is a multi-snapshot system, its systematic errors were defined slightly differently. While, the patterned linear polarizers' errors were treated in the same way, the rotating linear retarder errors were treated differently. The retardance error was assumed constant for all three snapshots, while the orientation errors were treated as a combination of a constant offset and a snapshot-specific error. This is done in parallel with the two dimensions of systematic error in Fig. 6. Single instantiations of reconstruction residuals are presented in Fig. 7 for the cross-diagonal combinations of errors.

Table 2 presents the verbose list of error configurations. Configuration 1 assumes the minimum number of lithographic masks necessary, while Configuration 2 assumes that every pixel within the MPA pattern has an independent selection of lithographic masks. The effect of the former is that correlated errors patterned over a detector lead to additional unintended channels, while the effect of the latter is a general increase in the noise floor within the Fourier domain. Figure 6 shows the effects of the two types of systematic errors for each MPA. When the systematic error is patterned, the empty channels shown in Fig. 1 are populated with unintended information. Looking at each MPA's effective channel structure makes it obvious that different MPAs will perform differently. Bachman's and Myhre's MPAs do not have any empty channels, and, thus, patterned systematic error is not expected to strongly affect the reconstruction accuracy—each channel will simply contain a slightly different linear combination of Stokes parameters. This can be accounted for by altering $\underline{\underline{\mathbf{Q}}}$. However, the other four MPAs rely on precise carrier construction to create empty channels. As a result, patterned errors will lead to crosstalk from unintended channels.

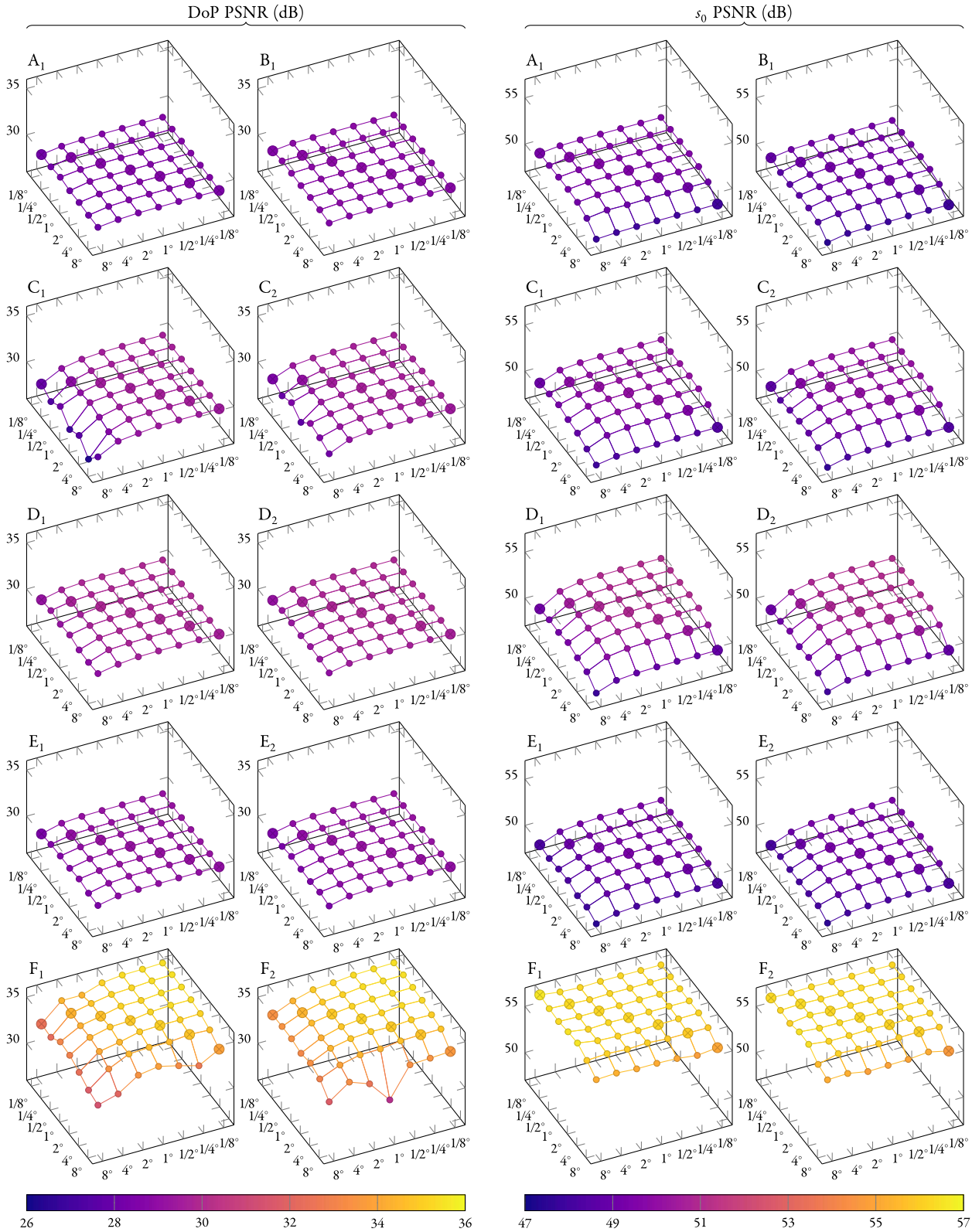

Fig. 6. MPA reconstruction accuracy as a function of systematic error. The angle amounts represent the standard deviations of the Gaussian-distributed perturbations added to the polarization element parameters implied by Table 2 and Fig. 5. The left dimension corresponds to random contribution to every pixel, while the right dimension corresponds to a random contribution to a pixel type within the MPA pattern. The larger marks on the cross-diagonal correspond to the combinations of random and patterned errors examined in Fig. 7.

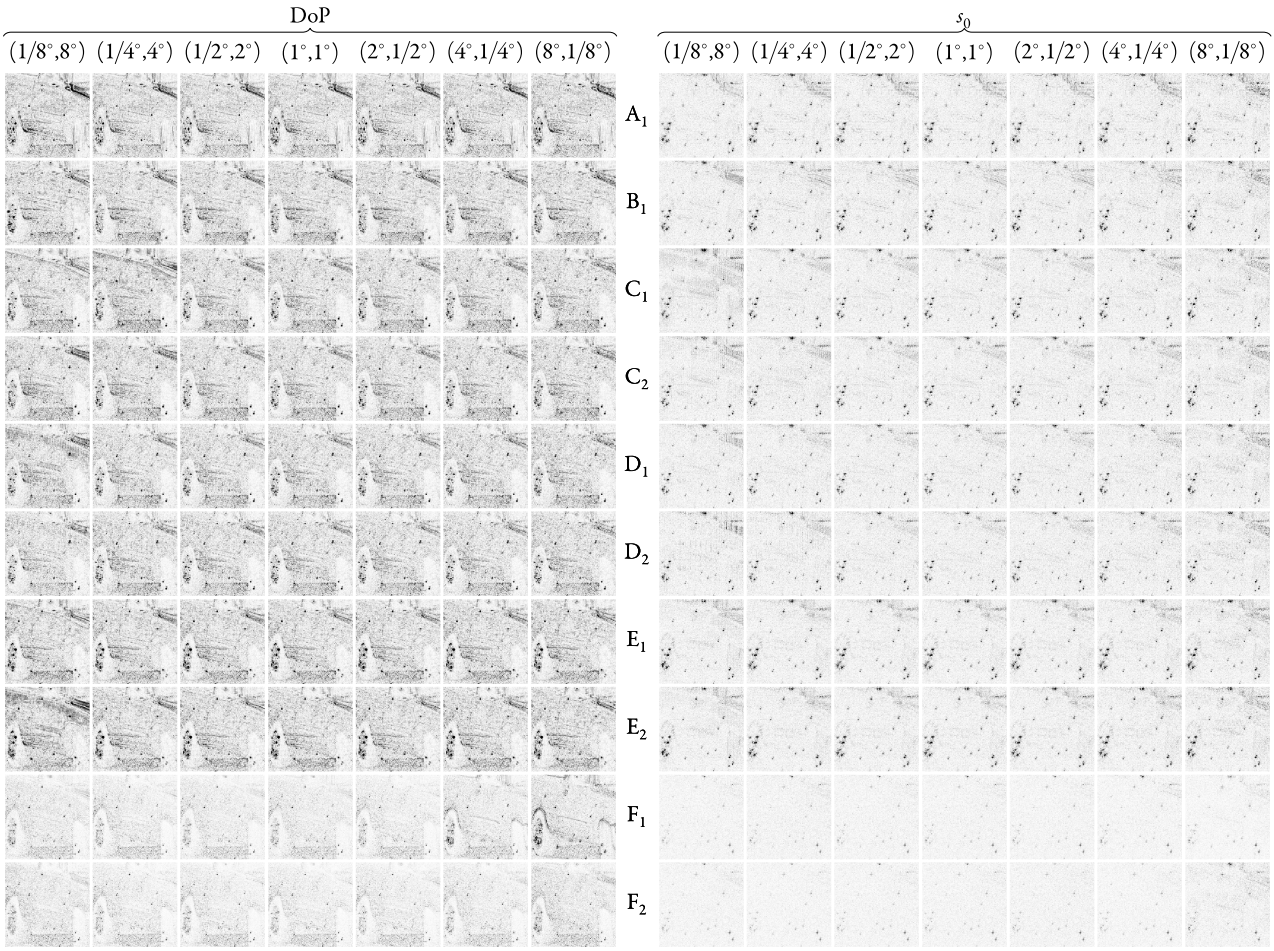

Fig. 7. Single instantiation reconstruction difference of DoP and s_0 from the 25 that were used in the systematic error analysis. Only seven of 49 error levels are shown—they form a cross-diagonal that trades off of the two error sources listed as (random systematic error, patterned systematic error). The images shown are of ROI # 1 from Fig. 2 and are normalized to the same levels as indicated in Fig. 3. SNR level of 30 dB is assumed for this exercise. MPA configurations are consistent with Table 2, Figs. 5 and 6.

4. DISCUSSION

A. Systematic Error-Free Case

As can be seen in Fig. 3, Bachman's MPA provides the lowest accuracy at all SNR levels, while Myhre's MPA and the new 3 × 3 MPA perform similarly with the former performing better in s_0 and the latter performing better in DoP at higher SNRs. Given that the 3 × 3 MPA introduces the extra need of partially polarized pixels without bringing a sizable performance advantage, it is of limited practical use. However, the negative result quantifies that focusing on bandwidth alone is not sufficient. Instead bandwidth and CN should be seen as equally important concepts in predicting system performance. The modified 2 × L MPAs yield the best single-snapshot s_0 and DoP accuracy. Higher L MPAs can extend s_1 and s_2 carriers further away from the s_0 carrier, and, because s_0 is likely to be of higher bandwidth than s_1 and s_2 [19], the 2 × 10 MPA yields higher reconstruction accuracy than the 2 × 4. However, for the foreseeable future, the modified 2 × 4 MPA is likely to remain the most manufacturable full-Stokes 2 × L MPA, as it only requires four different types of linear polarizers and retarders. It is of particular significance that its layout and channel structure are a combination of many separate elements: LeMaster and Hirakawa's micropolarizer orientations [18], Lukac's overall carrier structure [20,32], and adapted Myhre's linear retarder properties [24]. As the ability to apply many independent masks becomes more feasible, the modified 2 × 10 MPA will be better suited for typical polarization data. Finally, the 2 × 2 × 3 MPA has once again shown that a multi-snapshot design has the potential to deliver maximum bandwidth and reconstruction accuracy. Unlike the 2 × 2 × 2 MPA that has a very implementable ferroelectric liquid crystal rotator solution [19], the 2 × 2 × 3 MPA requires a more elaborate positioning of the retarder in front. As a result, it is not clear how much of the predicted performance will be obtainable. There are emerging technologies, such as the liquid crystal photonic transducers [33,34], that could pave the way for enabling this multi-snapshot design. The performance of the 2 × 2 × 3 MPA strongly depends on the successful implementation of the modulation design.

B. Non-zero Systematic Error Case

Under non-zero systematic error, Figs. 6 and 7 show that Bachman's and Myhre's MPAs do not suffer much in terms of DoP reconstruction accuracy, but do in terms of s_0

reconstruction accuracy. This is because the polarization channels are already multiplexed, and no unintended channels are created through inclusion of systematic error. The baseband, on the other hand, may start to include non-s_0 information leading to an overall reduction in the s_0 reconstruction's PSNR. The 2×4 MPA and the 2×10 MPA perform similarly, but, counter-intuitively, the 2×10 MPA performs more gracefully under systematic error. This is likely due to the fact that the 2×10 MPA has a greater number of pixel types, which implies a lesser impact of any individual correlated error distribution of one pixel type. This hypothesis is further supported by the fact that Configuration 2 MPAs generally perform better than Configuration 1 MPAs—correlated error is worse than independent error. Finally, despite the fact that the $2 \times 2 \times 3$ MPA's reconstruction performance degrades the most as systematic error goes up, its performance never dips below the performance of other MPAs.

5. CONCLUSION

In this paper, we have introduced two classes of full-Stokes MPAs: the very promising modified $2 \times L$ family, the largely unimpressive 3×3 MPA, as well as revisiting the extremely well performing $2 \times 2 \times 3$ MPA. The former two are spatially channeled polarimeters, whereas the latter is a hybrid temporally and spatially channeled polarimeter. We systematically examined the performance of these layouts and compared them with recently demonstrated full-Stokes MPA designs from the literature. By considering bandwidth along with SNR performance, the allocation of system bandwidth can be controlled to better suit the data at hand. Examining the new systems' performance under systematic error revealed their greater robustness. We further demonstrated the potential advantage of multi-snapshot designs that trade off spatial and temporal bandwidth to achieve even better performance in terms of both noise and error resiliency.

Besides the results presented here, we have recently found even more powerful ways of avoiding the emergence of unintended channels due to the existence of systematic error [35]. All existing hybrid-domain polarimeters use *separable* modulation strategies, where the modulation in the independent domains is accomplished using separate optical elements. In a *non-separable* system, an element such as a spatial light modulator can be used to modulate in two domains simultaneously in a way that is inseparably mixed. When this is the case, you no longer need a combination of modulation carriers to design the measurement's Fourier domain. Instead, the desired information-carrying channels can be located in arbitrary locations in the frequency domain via a single carrier, thus obviating the need for channel cancellation altogether. As further polarization-selection-device advancements become available, these techniques will enable additional gains through ensuring a complete absence of unintended channels.

Funding. Asian Office of Aerospace Research and Development (FA2386-15-1-4098).

Acknowledgment. IHIP data provided by Julia Craven and collected under funding by US DOE NNSA NA-22, Victoria Franques program manager.

REFERENCES

1. C. F. LaCasse, R. A. Chipman, and J. S. Tyo, "Band limited data reconstruction in modulated polarimeters," Opt. Express **19**, 14976–14989 (2011).
2. R. A. Chipman, "Polarimetry," in *Handbook of Optics*, 3rd ed. (McGraw-Hill, 2009), Chap. 15, Vol. **1**, pp. 15.1–15.46.
3. D. J. Diner, A. Davis, B. Hancock, G. Gutt, R. A. Chipman, and B. Cairns, "Dual-photoelastic-modulator-based polarimetric imaging concept for aerosol remote sensing," Appl. Opt. **46**, 8428–8445 (2007).
4. J. S. Tyo, C. F. LaCasse, and B. M. Ratliff, "Total elimination of sampling errors in polarization imagery obtained with integrated microgrid polarimeters," Opt. Lett. **34**, 3187–3189 (2009).
5. M. W. Kudenov, M. J. Escuti, N. Hagen, E. L. Dereniak, and K. Oka, "Snapshot imaging Mueller matrix polarimeter using polarization gratings," Opt. Lett. **37**, 1367–1369 (2012).
6. M. W. Kudenov, N. A. Hagen, E. L. Dereniak, and G. R. Gerhart, "Fourier transform channeled spectropolarimetry in the MWIR," Opt. Express **15**, 12792–12805 (2007).
7. T. Wakayama, T. Higashiguchi, H. Oikawa, K. Sakaue, M. Washio, M. Yonemura, T. Yoshizawa, J. S. Tyo, and Y. Otani, "Determination of the polarization states of an arbitrary polarized terahertz beam: vectorial vortex analysis," Sci. Rep. **5**, 9416 (2015).
8. C. F. LaCasse, T. Ririe, R. A. Chipman, and J. S. Tyo, "Spatio-temporal modulated polarimetry," Proc. SPIE **8160**, 81600K (2011).
9. I. J. Vaughn, O. G. Rodriguez-Herrera, M. Xu, and J. S. Tyo, "A portable imaging Mueller matrix polarimeter based on a spatio-temporal modulation approach: theory and implementation," Proc. SPIE **9613**, 961304 (2015).
10. A. S. Alenin and J. S. Tyo, "Generalized channeled polarimetry," J. Opt. Soc. Am. A **31**, 1013–1022 (2014).
11. R. M. A. Azzam, I. M. Elminyawi, and A. M. El-Saba, "General analysis and optimization of the four-detector photopolarimeter," J. Opt. Soc. Am. A **5**, 681–689 (1988).
12. D. S. Sabatke, M. R. Descour, E. L. Dereniak, W. C. Sweatt, S. A. Kemme, and G. S. Phipps, "Optimization of retardance for a complete Stokes polarimeter," Opt. Lett. **25**, 802–804 (2000).
13. J. S. Tyo, "Design of optimal polarimeters: maximization of signal-to-noise ratio and minimization of systematic error," Appl. Opt. **41**, 619–630 (2002).
14. J. S. Tyo, D. L. Goldstein, D. B. Chenault, and J. A. Shaw, "Review of passive imaging polarimetry for remote sensing applications," Appl. Opt. **45**, 5453–5469 (2006).
15. C. S. L. Chun, D. L. Fleming, and E. J. Torok, "Polarization-sensitive thermal imaging," Proc. SPIE **2234**, 275–286 (1994).
16. Z. Zhang, F. Dong, T. Cheng, K. Qiu, Q. Zhang, W. Chu, and X. Wu, "Nano-fabricated pixelated micropolarizer array for visible imaging polarimetry," Rev. Sci. Instrum. **85**, 105002 (2014).
17. C. F. LaCasse, J. S. Tyo, and R. A. Chipman, "Role of the null space of the DRM in the performance of modulated polarimeters," Opt. Lett. **37**, 1097–1099 (2012).
18. D. A. LeMaster and K. Hirakawa, "Improved microgrid arrangement for integrated imaging polarimeters," Opt. Lett. **39**, 1811–1814 (2014).
19. A. S. Alenin, I. J. Vaughn, and J. S. Tyo, "Optimal bandwidth micropolarizer arrays," Opt. Lett. **42**, 458–461 (2017).
20. I. J. Vaughn, A. S. Alenin, and J. S. Tyo, "Focal plane filter array engineering I: rectangular lattices," Opt. Express **25**, 11954–11968 (2017).
21. X. Zhao, A. Bermak, F. Boussaid, and V. G. Chigrinov, "Liquid-crystal micropolarimeter array for full Stokes polarization imaging in visible spectrum," Opt. Express **18**, 17776–17787 (2010).
22. K. A. Bachman, J. J. Peltzer, P. D. Flammer, T. E. Furtak, R. T. Collins, and R. E. Hollingsworth, "Spiral plasmonic nanoantennas as circular polarization transmission filters," Opt. Express **20**, 1308–1319 (2012).
23. J. J. Peltzer, K. A. Bachman, J. W. Rose, P. D. Flammer, T. E. Furtak, R. T. Collins, and R. E. Hollingsworth, "Plasmonic micropolarizers for full Stokes vector imaging," Proc. SPIE **8364**, 83640O (2012).
24. G. Myhre, W.-L. Hsu, A. Peinado, C. LaCasse, N. Brock, R. A. Chipman, and S. Pau, "Liquid crystal polymer full-Stokes division of focal plane polarimeter," Opt. Express **20**, 27393–27409 (2012).

25. W.-L. Hsu, G. Myhre, K. Balakrishnan, N. Brock, M. Ibn-Elhaj, and S. Pau, "Full-Stokes imaging polarimeter using an array of elliptical polarizer," Opt. Express **22**, 3063–3074 (2014).
26. X. Tu, O. J. Spires, X. Tian, N. Brock, R. Liang, and S. Pau, "Division of amplitude RGB full-Stokes camera using micro-polarizer arrays," Opt. Express **25**, 33160–33175 (2017).
27. J. S. Tyo and H. Wei, "Imaging polarimetry with imperfect optics," Appl. Opt. **45**, 5497–5503 (2006).
28. V. Gruev, J. V. der Spiegel, and N. Engheta, "Dual-tier thin film polymer polarization imaging sensor," Opt. Express **18**, 19292–19303 (2010).
29. I. J. Vaughn, A. S. Alenin, and J. S. Tyo, "A fast Stokes polarimeter: preliminary design," Proc. SPIE **10407**, 1040702 (2017).
30. J. Craven-Jones, M. W. Kudenov, M. G. Stapelbroek, and E. L. Dereniak, "Infrared hyperspectral imaging polarimeter using birefringent prisms," Appl. Opt. **50**, 1170–1185 (2011).
31. Z. Wang and A. C. Bovik, "Mean squared error: love it or leave it? A new look at signal fidelity measures," IEEE Signal Process. Mag. **26**, 98–117 (2009).
32. R. Lukac and K. N. Plataniotis, "Color filter arrays: design and performance analysis," IEEE Trans. Consum. Electron. **51**, 1260–1267 (2005).
33. Z. Brodzeli, L. Silvestri, A. Michie, Q. Guo, E. P. Pozhidaev, V. Chigrinov, and F. Ladouceur, "Sensors at your fibre tips: a novel liquid crystal-based photonic transducer for sensing systems," J. Lightwave Technol. **31**, 2940–2946 (2013).
34. J. Firth, Z. Brodzeli, M. Ciobotaru, T. Phung, F. Ladouceur, and L. Silvestri, "Accurate optical measurement of high voltage waveform using novel optical liquid crystal based sensor," Sens. Actuators A, Phys **268**, 164–172 (2017).
35. J. Song, A. S. Alenin, I. J. Vaughn, M. E. Gehm, and J. S. Tyo, "Channel-first design of modulated polarimeters," Proc. SPIE, 10655 (2018), accepted for presentation.